Applied Surface Science 580 (2022) 152278

Contents lists available at ScienceDirect

Applied Surface Science

journal homepage: www.elsevier.com/locate/apsusc

Full Length Article

Enhanced low-temperature catalytic performance for toluene combustion of CeO_2-supported Pt-Ir alloy catalysts

Yue Zhang [a], Cong Wu [b], Zhiqiang Wang [b], Jiawei Ji [a], Haiqin Wan [b], Weixin Zou [b], Qing Tong [a,*], Jingfang Sun [a], Lin Dong [a,b,*], Yu-Wen Chen [c]

[a] Key Laboratory of Mesoscopic Chemistry of MOE, School of Chemistry and Chemical Engineering, Jiangsu Key Laboratory of Vehicle Emissions Control, Center of Modern Analysis, Nanjing University, Nanjing, 210023, China
[b] School of the Environmental, Nanjing University, Nanjing, 210023, China
[c] Department of Chemical Engineering, National Central University, Jhong-Li, 32001, China

ARTICLE INFO

Keywords:
Pt-Ir alloy nanoparticle
Cerium dioxide
Toluene
Catalytic oxidation
Reaction pathway

ABSTRACT

Herein, bimetallic Pt-Ir alloy nanoparticles (NPs) were successfully fabricated by ethylene glycol reduction of $H_2PtCl_6{\cdot}6H_2O$ and $IrCl_3$ through a microwave-assisted method. The Pt-Ir alloy NPs were deposited on CeO_2 catalysts for toluene combustion. The $Pt_{2.5}Ir/CeO_2$ sample exhibited better catalytic activity at low reaction temperature, compared with monometallic catalysts. The excellent low-temperature catalytic activity was resulted from the interaction between Pt and Ir, richer adsorbed oxygen species and low-temperature reducibility. Furthermore, the in-situ DRIFTS was used to investigate the possible reaction pathway of $Pt_{2.5}Ir/CeO_2$. It showed that the broken of benzene ring on $Pt_{2.5}Ir/CeO_2$ can be accomplished at lower temperature, resulting in enhancing the deep oxidation of toluene.

1. Introduction

Toluene, one of the typical aromatic volatile organic compounds (VOCs), is widely used in the production of dyes, pesticides, spices and so on [1,2]. However, the emission of toluene will cause many problems for human health and environment. Many efforts have been done for the elimination of toluene [3], in which catalytic oxidation has attracted extensive attention due to its high efficiency and no secondary pollution [4,5]. Two main types of catalysts, transition metal oxides [6,7] and noble metal catalysts [8–14], have been applied to the catalytic combustion of toluene. Comparing with the transition metal oxides, supported noble metals are well-explored catalysts because of the superior catalytic activity [8].

Pt-based catalysts have been paid more attention in that they exhibit good catalytic activity for oxidation of toluene. Previous studies indicated that the catalytic activity of Pt-based catalysts for toluene combustion was related to the content of Pt^0 [9], the metal-support interaction [10], the dispersion of noble metal [11], etc. These factors can be designed by adjusting the electronic and geometric structure of catalysts [12]. And it can be easily achieved by adding another noble metal with different ratios, which has an influence on the catalytic performance of catalysts [13–15]. Some efforts have been made to study the Pt based alloy catalysts. Wu et al. [12] prepared the supported Au-Pt alloy catalyst, and it exhibited better catalytic activity compared with monometallic catalysts. Fu et al. [16] found that the synergistic effect between Pt and Pd resulted in the improvement of the catalytic activity for bimetallic Pt-Pd/MCM-41 catalyst. Pei et al. [17] prepared the PtRu alloy supported on 3DOM $Ce_{0.7}Zr_{0.3}O_2$ catalysts by different methods and found the existence of Ru was helpful to the low-temperature reducibility and oxygen adsorption ability of catalyst. Li et al. [18] found the interaction between bimetallic NPs and the metal-support interaction contributed to the enhancement of catalytic activity and stability for the supported Au-Pt alloy catalysts.

As one of platinum group elements, iridium can easily activate C-H bond and has good dispersibility on the surface of support [19], which has been gradually applied in the catalytic combustion of VOCs [20–22]. Sun et al. [20] investigated the influence of different electronic states on Ir-based catalysts for the oxidation of formaldehyde. The study found that Ir^0 can contribute to the activation of O_2 and the catalyst with higher content of Ir^0 showed a better performance. Ohtsuka et al. [21] found the existence of IrO_2 was positive for the stability of Pt/ZrO_2 for the oxidation of methane. Murciano et al. [22] investigated the catalytic

* Corresponding authors.
E-mail addresses: tongqing@nju.edu.cn (Q. Tong), donglin@nju.edu.cn (L. Dong).

https://doi.org/10.1016/j.apsusc.2021.152278
Received 24 September 2021; Received in revised form 7 December 2021; Accepted 17 December 2021
Available online 20 December 2021

property of bimetallic Au-Ir catalysts for toluene combustion. The electronic environment modified by iridium made a better performance for the bimetallic catalyst. However, the catalytic oxidation of toluene by Pt-Ir alloy catalyst has not been reported so far.

It is important to prepare the alloy NPs with well-defined structures. The alloy NPs prepared using the conventional heating method showed the mixed morphologies. Some studies [13,14] have reported that the alloy NPs with homogeneous structure were successfully formed with the microwave-assisted method. In addition, compared with the conventional heating method, microwave-assisted method [15] also showed the advantages of the fast reaction, well-distribute heating and high repeatability.

On the other hand, CeO_2 has the great oxygen storage capacity [23]. As active supporter, CeO_2 can not only play a role in dispersing and stabilizing NPs but also improving the redox ability and enhancing stability of supported noble metal catalysts, which contribute to the catalytic combustion of toluene [10]. Herein, we successfully employed CeO_2 supported Pt-Ir alloy NPs prepared by the microwaved-assisted ethylene glycol reduction method for toluene combustion in order to develop novel catalyst materials with prominent low-temperature activity and stability. It was found that the catalytic performance of alloy catalysts was better than the monometallic Pt or Ir. The $Pt_{2.5}Ir/CeO_2$ catalysts showed an excellent performance for toluene combustion with T_{50} was down to 121 °C. Additionally, the possible reaction mechanism was revealed by the *in-situ* DRIFTS test. In this work, we aim to synthesize the catalyst by an easy and effective strategy and provide a platform with good promise for the catalytic oxidation of toluene.

2. Experimental

2.1. Materials

Cerium nitrate hexahydrate ($Ce(NO_3)_3{\cdot}6H_2O$) and iridium chloride ($IrCl_3$) were purchased from Macklin. Chloroplatinic acid hexahydrate ($H_2PtCl_6{\cdot}6H_2O$) and polyvinyl pyrrolidone (PVP) were obtain from Aladdin. Ethylene glycol was obtained from Alfa Aesar. All chemical reagents were analytical grade and were used without further purification.

2.2. Catalysts preparation

The Pt_xIr NPs were synthesized by microwaved-assisted ethylene glycol reduction method. Pt_xIr NPs in different ratios can be obtained by adjusting the proportions of metal salt precursors. 15 mL ethylene glycol and 100 mg PVP were mixed and put into a 50 mL three-necked flask which was in a CEM-MARS-5 microwave reactor. When the temperature was stable at 150 °C, 3.0 mL mixture solution of $H_2PtCl_6{\cdot}6H_2O$ (0.02 M) and $IrCl_3$ (0.02 M) and 2.4 mL NaOH (0.25 M) were added to the three-necked flask. The reaction time was 30 min, and the solution was continuously stirred throughout the process. After the reaction, the reactants were immediately subjected to an ice water bath for 30 min. Acetone was used for centrifugation to remove the PVP, and then the product was washed by ethanol and n-hexane. The resulting product was dispersed and preserved in ethanol solution. Monometallic Pt and Ir were prepared by the same method.

CeO_2 was obtained by calcining cerium nitrate hexahydrate in muffle furnace at 500 °C for 5 h. The Pt_xIr NPs dispersed in ethanol solution were dropped into CeO_2 dispersed in ethanol solution. After stirring for 4 h, the product was evaporated by water bath, and then dried at 110 °C for 4 h. After grinding, the product was calcined at 200 °C for 2 h. Then it was reduced under H_2 atmosphere at 200 °C for 2 h. The obtained sample was denoted as Pt_xIr/CeO_2, and the real ratio was obtained by XRF.

2.3. Catalyst characterization

The real content of Pt and Ir in Pt_xIr/CeO_2 was detected by a ARL9800XP + X-ray fluorescence (XRF). X-ray diffraction (XRD) was used to study the crystalline structure of synthesized Pt_xIr NPs and Pt_xIr/CeO_2, and the results were recorded on a Philips X'Pert Pro diffractometer with Cu Kα radiation (λ = 0.15418 nm). The morphology and sizes of Pt_xIr were obtained by Transmission Electron Microscopy (TEM) on a JEM-2100 (voltage at 200 kV). The Pt_xIr alloys dispersed in ethanol was dripped and dried at carbon-film-supported copper grids. The morphology of Pt_xIr/CeO_2 was showed by High-angle annular dark-field scanning transmission electron microscopy (HAADF-STEM), and the distribution of Pt and Ir of Pt_xIr/CeO_2 was performed by the energy dispersive spectrometer (EDS) elemental mapping. The surface areas and pore volumes were obtained on a Micrometrics ASAP 2020 adsorption apparatus using the Brunauer-Emmett-Teller (BET) method. CO pulse chemisorption was used to obtain the dispersion of noble metals using a gas chromatogram (GC-5890). All the samples were reduced in 7 % H_2/N_2 at 200 °C for 2 h before measurement. Then the samples were heated under Ar atmosphere at 200 °C for 1 h. And when the temperature decreased to 30 °C, 5% CO/N_2 with a pulse mode was introduced until saturated adsorption. The stoichiometric ratio of CO/noble metal was assumed to be 1. X-ray photoelectron spectroscopy (XPS) analysis was recorded by a PHI 5000 Versa Probe system under monochromatic Al Kα radiation (1486.6 eV). The binding energies were determined by the adventitious carbon (C 1 s peak at 284.6 eV). The Raman spectroscopy was recorded on a LabRAM Arami spectrometer. And the laser excitation wavelength used was 532 nm. Temperature-programmed reduction was performed using a Finesorb-3010 instrument. The samples were first preheated under N_2 atmosphere at 200 °C for 1 h, after cooling at the room temperature, the samples were started to be heated to 700 °C in 7.0 % H_2/Ar flow at a rate of 10 °C /min. To study the reaction process for toluene combustion over Pt_xIr/CeO_2, *in-situ* Diffusion Reflectance Infrared Fourier Transform Spectra (*in-situ* DRIFTS) was carried out, which was recorded on a Nicolet iS50 FT-IR spectrometer using a mercury cadmium telluride (MCT) detector. The samples were preheated at 200 °C for 30 min in a N_2 stream (25 mL/min), and then the background patterns at the required temperature were collected during the cooling process. When the temperature was cooled at the room temperature, N_2 was replaced with 1000 ppm toluene. The patterns were recorded at the required temperature in the heating process.

2.4. Catalytic activity test

The as-prepared Pt_xIr/CeO_2 catalysts were used for the catalytic oxidation of toluene in a fixed-bed continuous flow quartz reactor with a space velocity of 15,000 mL $g^{-1}h^{-1}$. The reaction gas was formed from 1000 ppm toluene and air. The particle size of the catalyst was 20–40 mesh, and the dosage was 100 mg. The water vapor influence experiment was carried out by introducing 5 vol% H_2O into the mixture. Reactants and products were detected and analyzed online using a gas chromatography (GC-9869) with flame ionization detector (FID) and thermal conductivity detector (TCD). Toluene conversion ($X_{toluene}$, %) and the CO_2 selectivity (S_{CO2}, %) were defined as follows:

$$X_{toluene}(\%) = \frac{(C_{in} - C_{out})}{C_{in}} \times 100\% \quad (1)$$

$$S_{CO2}(\%) = \frac{C_{CO2}}{7(C_{in} - C_{out})} \times 100\% \quad (2)$$

C_{in} and C_{out} are the inlet and outlet toluene concentrations in the feed stream, respectively. C_{CO2} is CO_2 concentration in the outlet. T_{50} and T_{90} were used to evaluate the catalytic performances of the samples, which meant that the conversions of toluene were up to 50 and 90%, respectively.

The turnover frequency (TOF) was calculated as follows:

$$TOF\left(s^{-1}\right) = X \times \frac{C_0}{N_{noblemetal} \times D_{noblemetal}} \quad (3)$$

where × is toluene conversion at a certain temperature, C_0 (mol/s) is the initial toluene concentration per second, $N_{noble\ metal}$ (mol) and $D_{noble\ metal}$ (%) represent the molar amount and dispersion of Pt, Ir and Pt_xIr, respectively.

When the conversion of toluene was < 20%, the activation energy (Ea) was calculated as follows:

$$\ln r = -\frac{Ea}{RT} + \ln A \quad (4)$$

where r (mol s^{-1}) is the reaction rate, Ea (kJ mol^{-1}) is apparent activation energy and A is the pre-exponential factor.

3. Results and discussion

3.1. Texture and morphology properties

The molar ratios (x) of Pt/Ir were investigated by XRF test (shown in Table 1), with the values were 3.2, 2.5, 1.2, and 0.6, respectively.

Fig. 1 shows the XRD patterns of Pt, Ir and Pt_xIr samples. In comparison with the standard XRD patterns of Pt (JCPDS PDF#04–0802) and Ir (JCPDS PDF#46–1044), the Pt_xIr samples showed similar diffraction peaks, which were assigned to (111), (200), (220) and (311) lattice faces, indicating the face-centered cubic structures. It is worth noting that the diffraction peaks which were assigned to the (111) lattice plane continuously shifted to a lower value with the increase of Pt content. Meanwhile, the d-spacings of (111) reflection can be calculated by the Bragg equation (Table S1) and the results showed that the lattice spacings of (111) reflection of the Pt_xIr NPs were between Pt (111) and Ir (111), suggesting the formation of Pt_xIr alloy [24].

The microstructure of Pt_xIr samples was observed by TEM. It can be seen in Fig. 2 that the as-prepared samples were relatively uniform NPs. According to the statistical results of the sizes for different samples (Table S1), the average size of Pt was 2.36 nm and the average size of Ir was 1.31 nm. The average sizes of the as-prepared Pt_xIr alloys were similar, with the range of 2.1–2.2 nm. Lattice spacings can be measured from the HRTEM images. It showed that the lattice spacing of Pt and Ir samples were 2.27 Å and 2.22 Å, which were assigned to the (111) lattice plane of Pt and Ir, respectively. The lattice spacings of Pt_xIr alloys in the HRTEM images showed that the values of the lattice spacing were between Pt and Ir (Table S1), which proved that the alloys were formed, consistent with the XRD results.

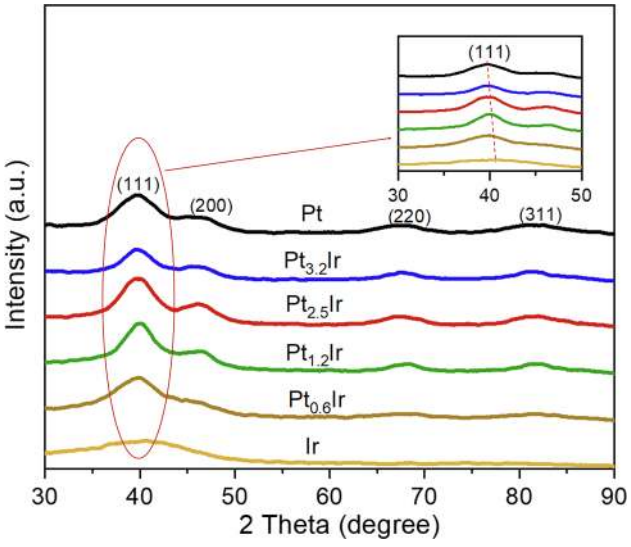

Fig. 1. XRD patterns of Pt, $Pt_{3.2}Ir$, $Pt_{2.5}Ir$, $Pt_{1.2}Ir$, $Pt_{0.6}Ir$ and Ir; Insert: expansion of the region contributed to the (111) lattice planes.

The XRD patterns of Pt/CeO_2, Ir/CeO_2 and Pt_xIr/CeO_2 samples are shown in Fig. S1. Compared with the standard pattern of lattice planes, the samples showed the same structure as cubic cerium dioxide. However, the diffraction peaks related to Pt or Ir were not observed in the XRD patterns, indicating the formation of the highly dispersed noble metal NPs. Fig. S2 showed that Pt/CeO_2, Ir/CeO_2 and Pt_xIr/CeO_2 samples all displayed type IV isotherms with H3 hysteresis loops, and the surface areas were concluded in Table 1. After loading the noble metals, the surface areas of Pt/CeO_2, Ir/CeO_2 and Pt_xIr/CeO_2 samples were slightly lower, with the values were in the range of 47.0–59.1 m^2/g.

In order to further study the dispersion state of Pt_xIr alloys on CeO_2, HAADF-STEM technique of Pt/CeO_2, Pt_xIr/CeO_2 and Ir/CeO_2 samples was carried out, as shown in Fig. S3. The average particle sizes of Pt_xIr alloys on CeO_2 were in the range of 2.4–2.6 nm (Table 1). It was found that the sizes of Pt_xIr alloys with different ratios showed no significant difference. It can be seen that Pt_xIr alloys had a good dispersibility on the surface of CeO_2. The distribution of Pt and Ir elements in $Pt_{2.5}Ir/CeO_2$ samples were studied by the EDS mapping, as shown in Fig. 3. The figures showed that Pt (red color) and Ir (yellow color) were uniformly dispersed and mixed on CeO_2 (green color), which further proved the formation of the alloys [25].

3.2. Catalytic activity

Fig. 4 (a) shows the catalytic combustion curves of Pt/CeO_2, Pt_xIr/CeO_2 and Ir/CeO_2 samples for toluene conversion. In order to show the catalytic activities of the samples readily, T_{50} and T_{90} were compared (Table 2). Comparing with Ir/CeO_2 sample, when Pt metal was added, the catalytic activity was significantly improved and the catalytic activity of toluene oxidation increased at first and then decreased with increase of the Pt content. The $Pt_{2.5}Ir/CeO_2$ sample exhibited the highest catalytic activity for toluene combustion, with T_{50} = 121 °C and T_{90} = 139 °C, which were lower than those of the monometallic Pt/CeO_2 (T_{50} = 131 °C and T_{90} = 148 °C) and Ir/CeO_2 (T_{50} = 188 °C and T_{90} = 217 °C) samples. Fig. S4 (a) shows the CO_2 selectivity of the Pt/CeO_2, Pt_xIr/CeO_2 and Ir/CeO_2 samples. And it showed that the selectivity of CO_2 was increased with the temperature and reached 100% at about 160 °C, indicating that toluene was uncompleted oxidation at low temperature. Furtherly, the $Pt_{2.5}Ir/CeO_2$ sample exhibited the best selectivity of CO_2, which was consistent with the result of toluene conversion. Figure S4 (b) shows the Arrhenius plots for the oxidation of toluene over Pt_xIr/CeO_2, Pt/CeO_2, and Ir/CeO_2, and the results (Table 2) showed that $Pt_{2.5}Ir/CeO_2$ had a lowest activation energy value, suggesting that toluene was easier oxidized on the $Pt_{2.5}Ir/CeO_2$ [9]. In order to study the intrinsic activity of Pt/CeO_2, Pt_xIr/CeO_2 and Ir/CeO_2 samples, the reaction rate and turnover frequencies (TOFs) of toluene combustion at 110 °C were determined for toluene combustion, shown in Table 2. The values were in order of $Pt_{2.5}Ir/CeO_2$ > $Pt_{1.2}Ir/CeO_2$ > $Pt_{3.2}Ir/CeO_2$ > Pt/CeO_2 > $Pt_{0.6}Ir/CeO_2$ > Ir/CeO_2. It is evident that the $Pt_{2.5}Ir/CeO_2$ sample exhibited the highest reaction rate (11.27 μmol/ (g_{cat} s)) and the highest TOF value ($5.02 \times 10^{-3}\ s^{-1}$) at 110 °C. Compared with other studies for the catalytic oxidation of toluene summarized in Table S2, $Pt_{2.5}Ir/CeO_2$ showed an excellent low-temperature activity, indicating a good applying potential.

The stability of catalyst also plays an important role for evaluating the practical application as well as the toluene conversion. Therefore, the water resistance and stability tests for $Pt_{2.5}Ir/CeO_2$, Pt/CeO_2 and Ir/CeO_2 samples were carried out at 160 °C with 1000 ppm toluene and a certain SV of 15000 mL $g^{-1}h^{-1}$. As shown in Fig. 4(b), after the introduction of H_2O into the reaction system, the toluene conversion of $Pt_{2.5}Ir/CeO_2$, Pt/CeO_2 and Ir/CeO_2 samples showed no obvious change, suggesting that the addition of H_2O had limited impact on the catalytic

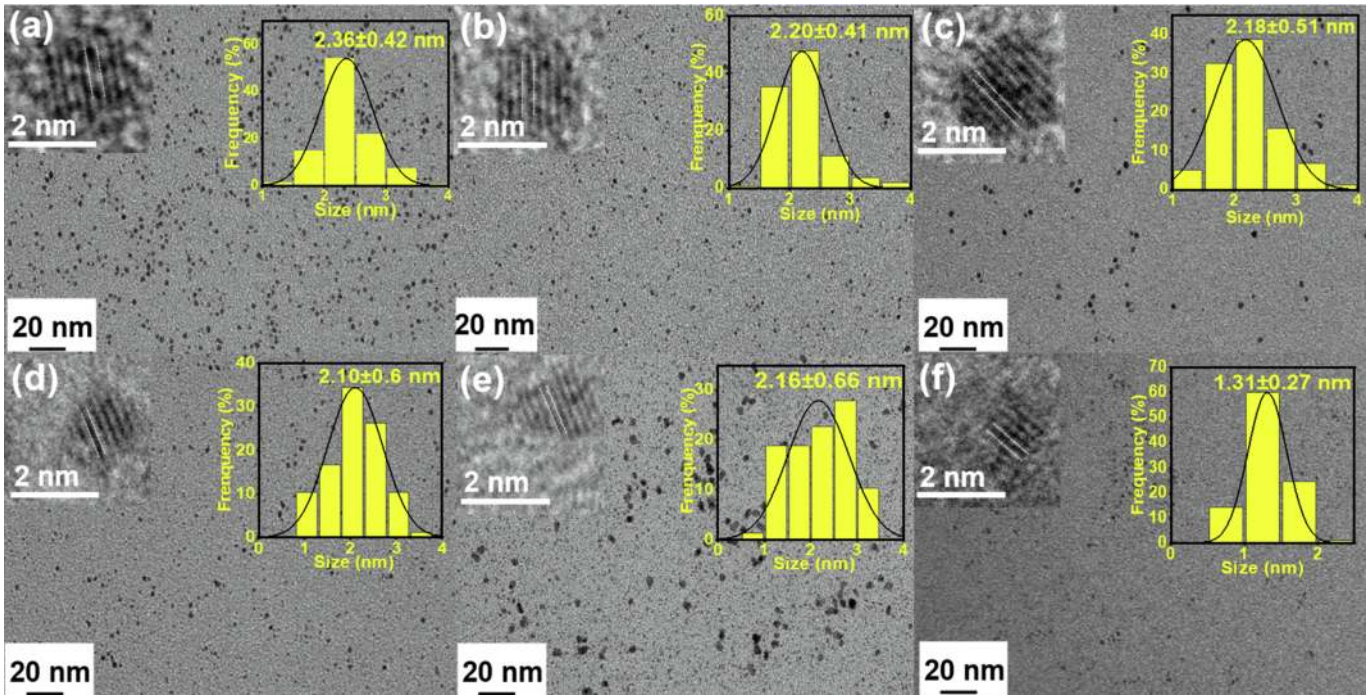

Fig. 2. TEM images of (a) Pt (b) $Pt_{3.2}Ir$ (c) $Pt_{2.5}Ir$ (d) $Pt_{1.2}Ir$ (e) $Pt_{0.6}Ir$ (f) Ir; Insets: HRTEM images and size distribution histograms.

Table 1
The actual metal contents, noble metal particle sizes, and BET data for samples.

Sample	Actual Pt content[a] (wt%)	Actual Ir content[a] (wt%)	Real Pt/Ir molar ratio[a] (mol/mol)	Noble metal particle size[b] (nm)	BET surface area[c] (m^2/g)	Pore volume[c] (cm^3/g)
Pt/CeO_2	0.41	–	–	2.66	59.1	0.211
$Pt_{3.2}Ir/CeO_2$	0.32	0.10	3.2	2.41	51.3	0.200
$Pt_{2.5}Ir/CeO_2$	0.35	0.14	2.5	2.60	47.0	0.185
$Pt_{1.2}Ir/CeO_2$	0.24	0.20	1.2	2.58	54.7	0.200
$Pt_{0.6}Ir/CeO_2$	0.16	0.27	0.6	2.38	51.2	0.191
Ir/CeO_2	–	0.41	–	1.48	51.2	0.196
CeO_2	–	–	–	–	64.7	0.220

a Data were determined by the XRF test.
b Data were measured according to the HAADF-STEM images of Pt/CeO_2, Pt_xIr/CeO_2 and Ir/CeO_2.
c Data were obtained according to the BET method.

performance of $Pt_{2.5}Ir/CeO_2$, Pt/CeO_2 and Ir/CeO_2. Fig. 4(c) showed the catalytic performance of $Pt_{2.5}Ir/CeO_2$, Pt/CeO_2 and Ir/CeO_2 samples in reaction flow for 30 h at 160 °C. All catalysts remained good catalytic activity in reaction flow for 30 h, indicating an excellent catalytic stability.

3.3. Surface oxygen vacancy/adsorbed oxygen species

To connect the catalytic performance with the Pt/Ir ratios, a series of characterization methods have been done to investigate the properties of the catalysts. It is generally believed that the increase of surface oxygen vacancy concentration is beneficial to the adsorption and activation of oxygen, which is conducive to the catalytic oxidation of toluene [26,27]. Therefore, in order to investigate the surface oxygen vacancies and adsorbed oxygen species of the samples with different Pt/Ir ratios, Raman spectra were first measured, as shown in Fig. 5 (a). The peak of CeO_2 at 464 cm^{-1} was attributed to the F_{2g} mode peak of CeO_2 [28]. The peak at 595 cm^{-1} was attributed to the defect (D) mode of CeO_2 which was related to the oxygen vacancy or anion defect in the CeO_2 fluorite structure [29], and the peak at 833 cm^{-1} was attributed to the surface adsorption O^{2-} vibration which was related to the existence of oxygen vacancy [30]. After loading noble metals, the peak at 595 cm^{-1} showed a blue shift and the peak continuously shifted to a higher value with the increase of Ir content, indicating the interaction between noble metals and CeO_2 [31]. The relative concentration of surface oxygen vacancies could be represented by I_D/I_{F2g} (Table 3). It would reveal that the relative concentration of surface oxygen vacancies increased significantly after the deposition of Pt, Ir or Pt_xIr alloy particles, indicating that the noble metals can help to increase the concentration of surface oxygen vacancies on CeO_2-supported catalysts. The highest relative concentration of surface oxygen vacancy on $Pt_{2.5}Ir/CeO_2$ could be one of the main reasons for its superior toluene oxidation activity. In addition, the peaks of Ir/CeO_2 sample at 550 cm^{-1} and 728 cm^{-1} belonged to Ir-O [32]. However, the peak at 550 cm^{-1} gradually shifted to lower wavenumber [4,33] and the peak at 728 cm^{-1} decreased gradually with the increase of Pt content. These phenomena indicated that there was an interaction between Pt and Ir.

It has been reported that the formation of Ce^{3+} was always related to the generation of oxygen vacancies [26] and then the Ce 3d XPS spectra were discussed. As to the Ce 3d spectra (Fig. 5 (b)), the binding energy (BE) = 900.7, 903.0, 907.4 and 916.5 eV were assigned to the Ce $3d_{3/2}$ orbital, and the BE = 882.2, 885.0, 888.8, and 898.2 eV were associated with the Ce $3d_{5/2}$ orbital [34]. The BE = 885.0 and 903.0 eV were assigned to the surface Ce^{3+} species, and the BE = 882.2, 888.8, 898.2, 900.7, 907.4 and 916.5 eV were attributed to the surface Ce^{4+} species [28–35]. Therefore, all samples contained Ce^{3+} and Ce^{4+} and the Ce^{3+} contents were in the order of $Pt_{2.5}Ir/CeO_2$ > $Pt_{1.2}Ir/CeO_2$ > $Pt_{0.6}Ir/CeO_2$ > Ir/CeO_2 > $Pt_{3.2}Ir/CeO_2$ > Pt/CeO_2. The results showed that Pt_xIr/CeO_2 exhibited more surface oxygen vacancies compared with Pt/CeO_2, which agreed with Raman. The O 1 s spectra are shown in Fig. 5 (c). The BE = 529.1, 531.6 and 533.1 eV are assigned to the surface lattice oxygen (O_{latt}), surface adsorbed oxygen (O_{ads}) and carbonate or adsorbed

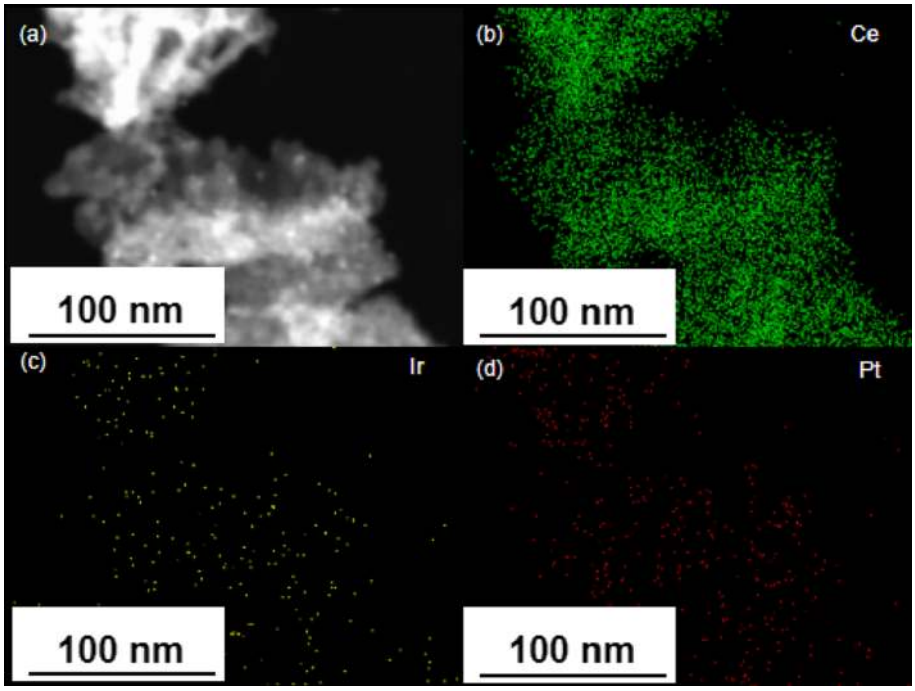

Fig. 3. (a) HAADF-STEM image of $Pt_{2.5}Ir/CeO_2$ (b-d) EDS elemental mapping images of $Pt_{2.5}Ir/CeO_2$.

molecular water (O_{-OH}) [36], respectively. The content of the O_{ads} species was in the order of $Pt_{2.5}Ir/CeO_2 > Pt_{1.2}Ir/CeO_2 > Pt_{0.6}Ir/CeO_2 > Ir/CeO_2 > Pt_{3.2}Ir/CeO_2 > Pt/CeO_2$, which corresponded to the results of Ce 3d. It indicated that Pt_xIr/CeO_2 had stronger ability to activate oxygen [37] when Ir was added.

From the results described above, it can be seen that $Pt_{2.5}Ir/CeO_2$ sample had the highest oxygen vacancies among all samples, which might contribute to the excellent activity. However, the order of the surface oxygen vacancies or O_{ads} were inconsistent with that of catalytic activity, shown in Fig. S5. It suggests that the surface oxygen vacancies contribute to the catalytic activity, but it was not the decisive factor for toluene combustion. Zhang et al [38] reported that the Pt^0 species also plays an important role besides surface oxygen vacancies for toluene combustion over Pt catalysts. Therefore, other factors need to be analyzed for comprehensive consideration besides surface oxygen vacancies.

3.4. The interaction between Pt and Ir and the low-temperature reducibility properties

In order to study the interaction between Pt and Ir, Ir4f and Pt4f XPS spectra were discussed. Fig. 6 (a) shows the Ir 4f spectra, which are composed of Ir $4f_{7/2}$ and Ir $4f_{5/2}$ [39,40]. There were two species in the spectra: the BE = 60.6 ($4f_{7/2}$) and 63.6 eV ($4f_{5/2}$) were assigned to Ir^0, and the BE = 61.4 ($4f_{7/2}$) and 64.5 eV ($4f_{5/2}$) were assigned to $Ir^{\delta+}$ [41]. Comparing with Ir/CeO_2 sample, the binding energy of Pt_xIr/CeO_2 samples shifted towards lower BE's, suggesting that the electrons transferred from Pt to Ir [42,43]. The result indicated that there was an interaction between Pt and Ir, which agreed with the Raman spectra. It is generally believed that Ir^0 species is helpful to the activation of O_2 due to it can donate electrons to the antibonding π^* orbital of O_2 [23,44]. Therefore, the state of Ir in the catalysts is also important. We can see from the Table 3, it was apparent that the molar ratio of Ir^0 increased by adding Pt as comparing with the Ir/CeO_2 sample, which could be attributed to the electrons gained by Ir from Pt. And the molar ratio of Ir^0 showed the same order with the O_{ads}, as shown in Fig. S5. Therefore, the alloying of Pt and Ir promotes the increase of Ir^0 species which facilitates the activation of oxygen in the catalytic oxidation of toluene.

Fig. 6 (b) shows the Pt 4f spectra. Three types of species are observed in the spectra: the ones at BE = 70.6 eV ($4f_{7/2}$) and 73.9 eV ($4f_{5/2}$) were assigned to the surface metallic Pt (Pt^0) species; the ones at BE = 71.7 eV ($4f_{7/2}$) and 75.3 eV ($4f_{5/2}$) were attributed to the surface Pt^{2+} species; and the ones at BE = 73.6 eV ($4f_{7/2}$) and 77.3 eV ($4f_{5/2}$) were ascribed to the surface Pt^{4+} species [45–47]. It was observed that the Pt 4f peaks of the Pt_xIr/CeO_2 samples shifted to higher BE's with the increase of Ir, which was consistent with Ir 4f spectra. In addition, Pt^0 is often considered as an active specie in the catalytic oxidation of toluene [48,49] and some studies have shown that Pt^0 species is helpful for the adsorption of toluene [9,50]. It was found that the $Pt_{2.5}Ir/CeO_2$ sample contained the highest content of Pt^0 (Table 3) and the order was consistent with the catalytic activity (Fig. S5), which indicated that the catalytic activity of the samples was related to the molar ratio of Pt^0. Therefore, adjusting the ratio of Pt and Ir can change the interaction between Pt and Ir of catalysts, and influence the adsorption of toluene and oxygen activation, which contribute to the catalytic oxidation of toluene.

The reduction properties of Pt_xIr/CeO_2 samples with different Pt/Ir ratios were determined by H_2-TPR, as shown in Fig. 6 (c) The reduction peaks of the CeO_2 were at 208 °C and 452 °C, which were attributed to the reduction of surface oxygen and subsurface oxygen [51,52], respectively. Compared with CeO_2, the reduction temperature of surface oxygen on Pt_xIr/CeO_2 sample was reduced to 117 ~ 155 °C, indicating noble metals affected the reduction of surface oxygen of CeO_2. Besides, new reduction peaks below 110 °C appeared when Pt, Ir or Pt_xIr were loaded on CeO_2, which was associated to the reduction of PtO_x or IrO_x species [53,54]. Compared with Pt/CeO_2 and Ir/CeO_2 samples, the reduction peaks of Pt_xIr/CeO_2 samples shifted and showed reduction peaks at different temperature locations with different Pt content in alloys, suggesting there was an interaction between Pt and Ir. Among them, $Pt_{2.5}Ir/CeO_2$ sample had the lowest reduction temperature. The results indicated a certain value of Pt/Ir contributed to improving the reducibility of catalyst. To sum up, it was reasonable to suggest that the $Pt_{2.5}Ir/CeO_2$ sample exhibited the high catalytic activity in connection with the good low temperature reduction ability [34].

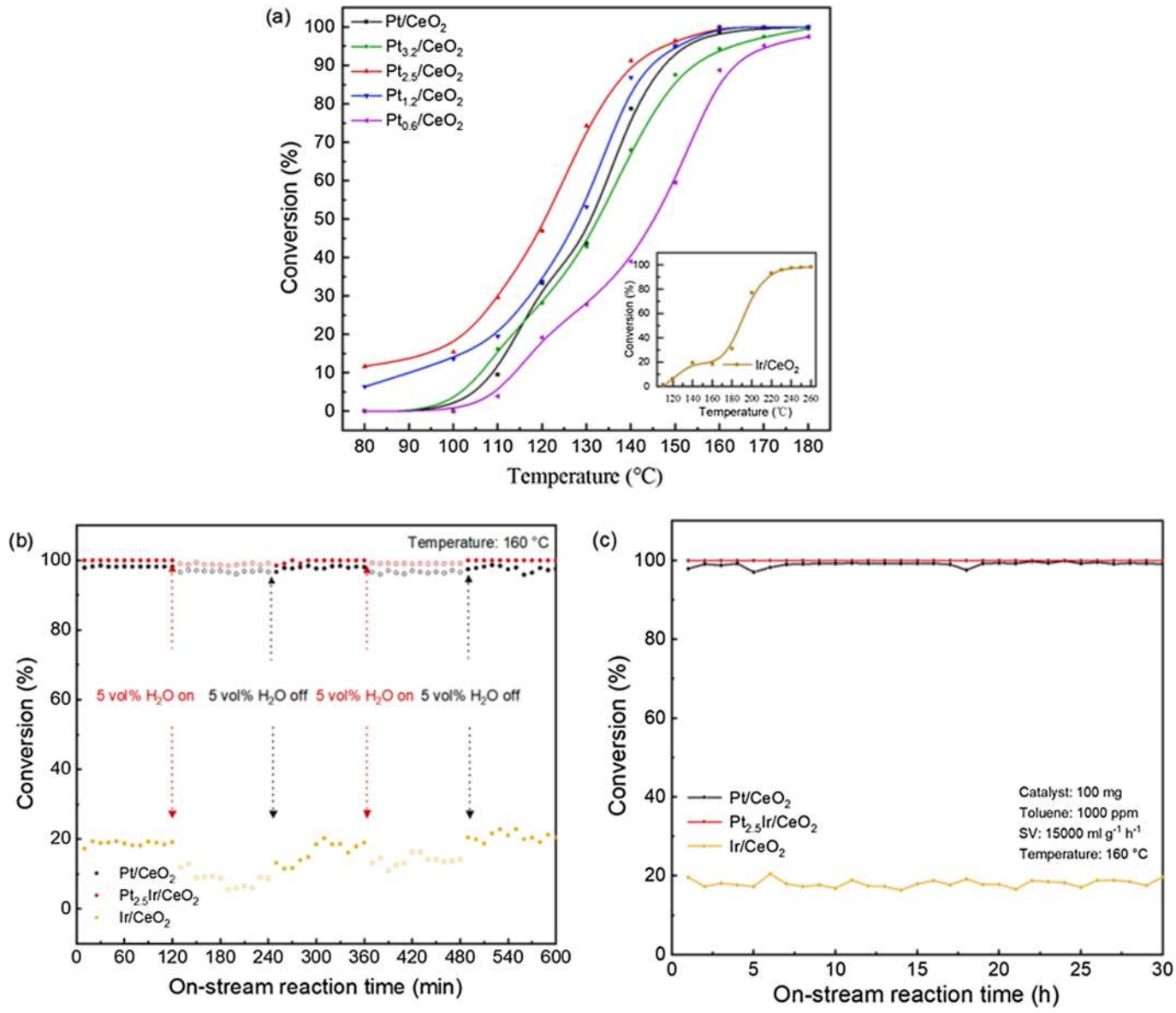

Fig. 4. (a) Conversion of toluene over Pt/CeO_2, Pt_xIr/CeO_2 and Ir/CeO_2. Toluene concentration: 1000 ppm; SV: 15,000 mL $g^{-1}h^{-1}$; catalyst amount: 100 mg. (b) Effect of H_2O of $Pt_{2.5}Ir/CeO_2$, Pt/ CeO_2 and Ir/ CeO_2 (c) stability during 30 h of toluene oxidation of $Pt_{2.5}Ir/CeO_2$, Pt/ CeO_2 and Ir/ CeO_2.

Table 2
Catalytic performances for Pt/CeO_2, Ir/CeO_2 and Pt_xIr/CeO_2.

Samples	Catalytic activity		Metal dispersion (%)	Specific reaction rate at 110 °C (μmol/ (g_{cat} s))	$TOF_{Noble\ metal}$ at 110 °C (10^{-3} s^{-1})	Ea (KJ/ mol)
	T_{50} (°C)	T_{90} (°C)				
Pt/CeO_2	131	148	54.0	4.29	1.56	67.9
$Pt_{3.2}Ir/CeO_2$	132	155	46.8	6.99	2.90	74.7
$Pt_{2.5}Ir/CeO_2$	121	139	43.6	11.27	5.02	54.4
$Pt_{1.2}Ir/CeO_2$	128	145	45.2	8.16	3.45	57.0
$Pt_{0.6}Ir/CeO_2$	145	164	70.7	1.61	0.43	85.3
Ir/CeO_2	188	217	81.4	–	–	115.4

3.5. Proposed reaction mechanism

For the purpose of studying the catalytic oxidation mechanism of toluene on $Pt_{2.5}Ir/CeO_2$ sample, *in-situ* DRIFTS test was carried out under different temperatures (Fig. 7 (a)). At 40 °C, the bands detected at 3080 and 3026 cm^{-1} were assigned to v(C-H) of the aromatic ring [55], 1602 and 1494 cm^{-1} belonged to skeleton vibrations of the aromatic ring [56]. The bands at 1177 and 1026 cm^{-1} were respectively attributed to asymmetric C-C stretching vibration and C-H bending vibration of aromatic ring [57,58]. These bands implied that toluene was adsorbed on the surface of the catalyst. The bands at 2924 and 2878 cm^{-1} were assigned to symmetric and asymmetric stretching vibrations of methylene [59], 1192 and 1081 cm^{-1} belonged to C-O stretching vibration of alkoxide species, which indicated the adsorbed toluene was partially oxidized to benzyl alcohol (C_6H_5-CH_2O-) species [60,61]. In addition, the weak bands detected at 1668 and 1698 cm^{-1} [62,63] were attributed to the asymmetrical stretching of C = O, 1557 and 1541 cm^{-1} [64] belonged to the asymmetric v(COO) stretching vibrations. These weak bands suggested that benzaldehyde and benzoate were also formed. When the temperature increased, the benzoate was

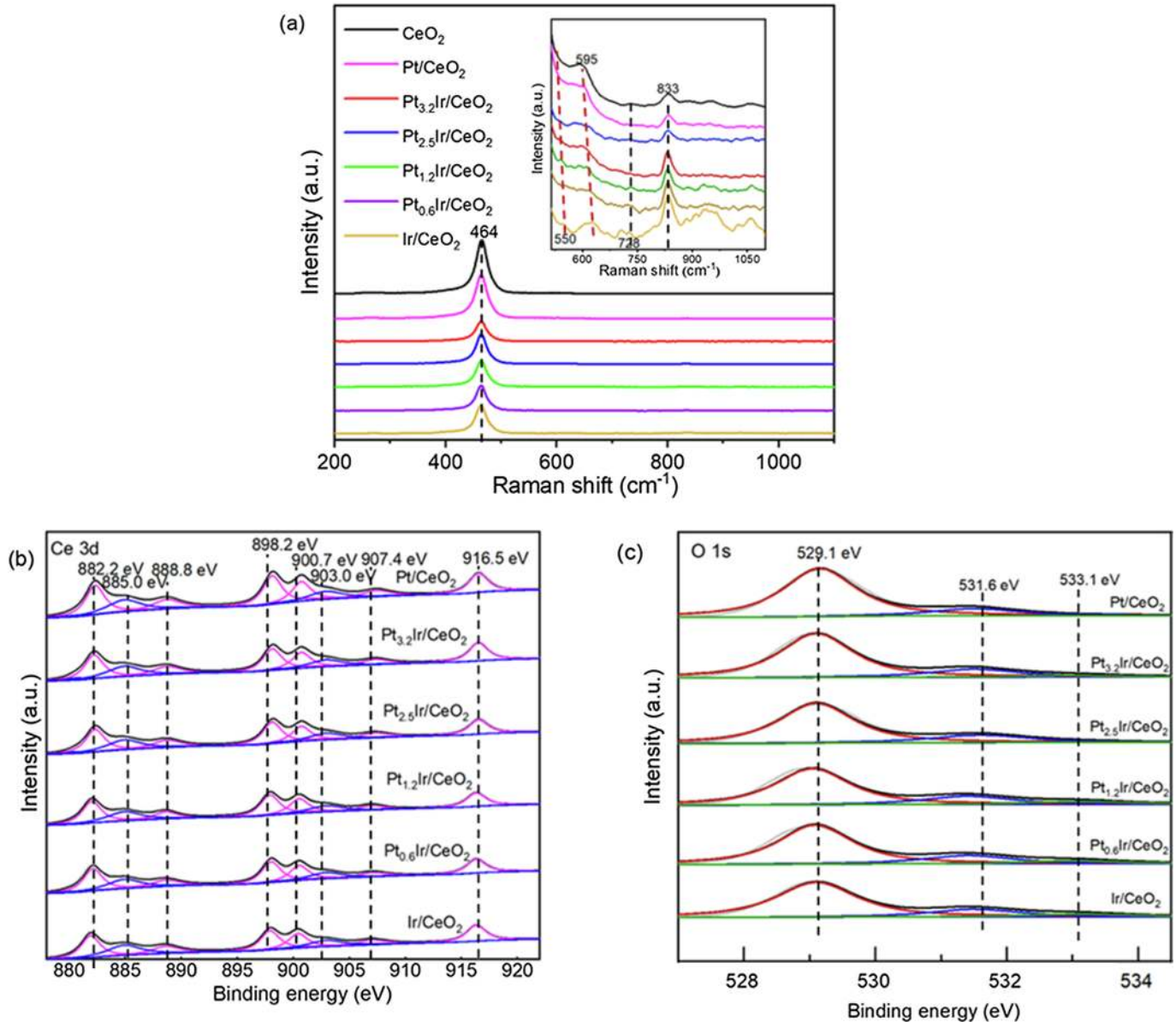

Fig. 5. (a) Raman profiles of CeO_2, Pt/CeO_2, Pt_xIr/CeO_2 and Ir/CeO_2. (b-c) Ce 3d, O 1 s XPS spectra of Pt/CeO_2, Pt_xIr/CeO_2 and Ir/CeO_2.

Table 3
The Raman and XPS data of Pt/CeO_2, Pt_xIr/CeO_2 and Ir/CeO_2.

catalyst	I_D/I_{2g}	surface element composition					
		$Ce^{3+}/(Ce^{3+}+Ce^{4+})$ (%)	$Q_{ads}/(Q_{ads}+Q_{latt})$ (%)	$Pt^0/(Pt^0+Pt^{2+}+Pt^{4+})$ (%)	$Pt^{2+}/(Pt^0+Pt^{2+}+Pt^{4+})$ (%)	$Pt^{4+}/(Pt^0+Pt^{2+}+Pt^{4+})$ (%)	$Ir^0/(Ir^0+Ir^{\delta+})$ (%)
Pt/CeO_2	0.0187	23.7	12.5	63.8	26.3	9.9	–
$Pt_{3.2}Ir/CeO_2$	0.0187	24.2	15.6	61.8	24.4	13.8	27.5
$Pt_{2.5}Ir/CeO_2$	0.0220	25.8	17.9	66.6	18.3	15.1	44.8
$Pt_{1.2}Ir/CeO_2$	0.0216	25.3	17.4	64.4	19.1	16.5	42.2
$Pt_{0.6}Ir/CeO_2$	0.0188	24.9	17.2	56.0	22.9	21.1	38.6
Ir/CeO_2	0.0187	24.8	17.0	–	–	–	14.5
CeO_2	0.0160	–	–	–	–	–	–

accumulated on the surface of the catalysts. At 120 °C, the characteristic bands of toluene disappeared and several bands at 1359, 1371, 1394, 1441, 1507 and 1733 cm^{-1} peaks were observed. Among them, the bands at 1733 cm^{-1} were attributed to the asymmetric C = O stretching vibrations, indicating the existence of ketone or aldehyde without aromatic conjugation [65], and the bands at 1394 and 1359 cm^{-1} belonged

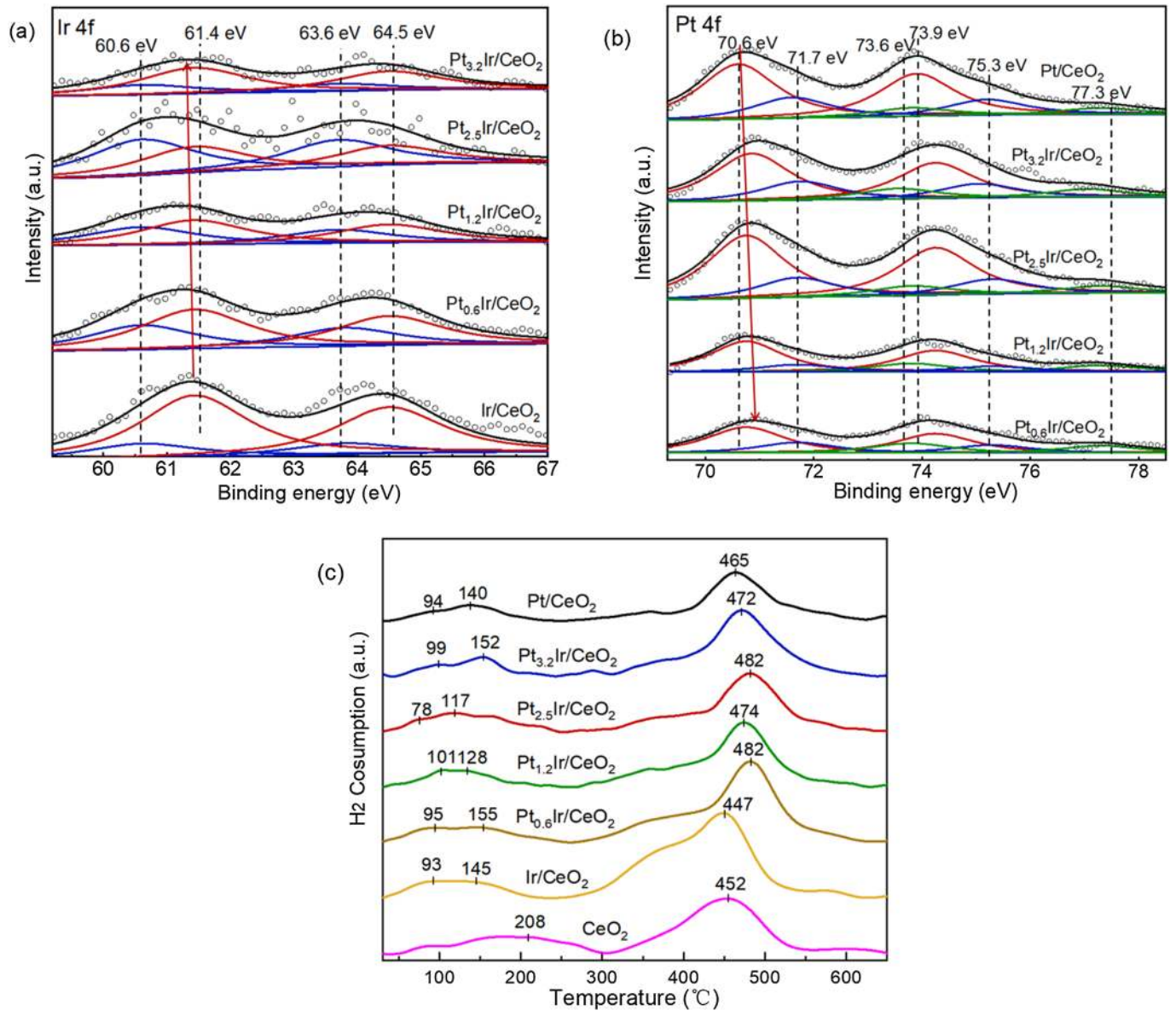

Fig. 6. (a-b) Ir 4f, Pt 4f XPS spectra of Pt/CeO_2, Pt_xIr/CeO_2 and Ir/CeO_2; (c) H_2-TPR profiles of CeO_2, Pt/CeO_2, Pt_xIr/CeO_2, and Ir/CeO_2.

to formate ($HCOO^-$) or monodentate carbonate species and symmetric v (COO) stretching [57], respectively. The bands at 1441 and 1507 cm^{-1} were assigned to maleates [66]. In addition, the bands at 1367 cm^{-1} belonged to the symmetrical deformation vibration of methyl, suggesting the existence of acetone [67]. These results showed that benzoate was further oxidized and the benzene ring was broken. When the temperature increased, these intermediate products were accumulated and CO_2 (2360 cm^{-1}, 2324 cm^{-1}) was detected [59]. Therefore, the possible mechanism of toluene on $Pt_{2.5}Ir/CeO_2$ sample was as follows: Firstly, toluene was adsorbed on the active site Pt^0, then toluene was rapidly oxidized to benzyl alcohol, benzoate and benzaldehyde by the active oxygen species which were related to the surface oxygen vacancies and Ir^0 species. At 120 °C, the benzene ring was broken, benzoic acid was further oxidized to maleates, formate and acetone. Finally, these intermediate products were oxidized to CO_2 and H_2O.

In order to make a comparison, we also carried out *in-situ* DRIFTS of Pt/CeO_2 and Ir/CeO_2 samples at different temperatures. Fig. 7 (b) shows the *in-situ* DRIFTS spectra of Pt/CeO_2 sample. The typical peaks of toluene at 1599, 1498 cm^{-1} were detected, suggesting toluene was absorbed on the catalyst [56]. The bands detected at 1184, 1081, 1024 cm^{-1} could be attributed to the existence of benzyl alcohol species, 1559, 1541 cm^{-1} could be attributed to the existence of benzoate [60,64] and the bands at 1698 cm^{-1} belonged to the peaks of benzaldehyde [62]. It was worth noting that the bands at 1357, 1371, 1394, 1444, 1506 cm^{-1} were detected at 140 °C, suggesting the benzene ring was broken and formate, maleate and acetone [57,66] were formed at higher temperature compared with $Pt_{2.5}Ir/CeO_2$, which indicated that the catalytic oxidation ability of Pt/CeO_2 was weaker than that of $Pt_{2.5}Ir/CeO_2$, consistent with the XPS and Raman results. When temperature increased, CO_2 (2360 cm^{-1}, 2324 cm^{-1}) was detected.

The *in-situ* DRIFTS spectra of Ir/CeO_2 sample are shown in Fig. 7 (c). The bands at 1600 cm^{-1} and 1496 cm^{-1} could be attributed to the absorbed toluene on the catalyst. The bands detected at 1025, 1068, 1196, 1540, 1560, 1697 cm^{-1} suggested that toluene was partially oxidized to benzyl alcohol, benzoic acid and benzaldehyde. And the characteristic peaks of formate (1394 cm^{-1}, 1359 cm^{-1}), maleate (1507 cm^{-1}, 1445 cm^{-1}) and acetone (1370 cm^{-1}) appeared at 160 °C, which could be detected at lower temperature on the $Pt_{2.5}Ir/CeO_2$. When the temperature increased, these intermediate products were accumulated, and CO_2 (2360 cm^{-1}, 2324 cm^{-1}) was detected.

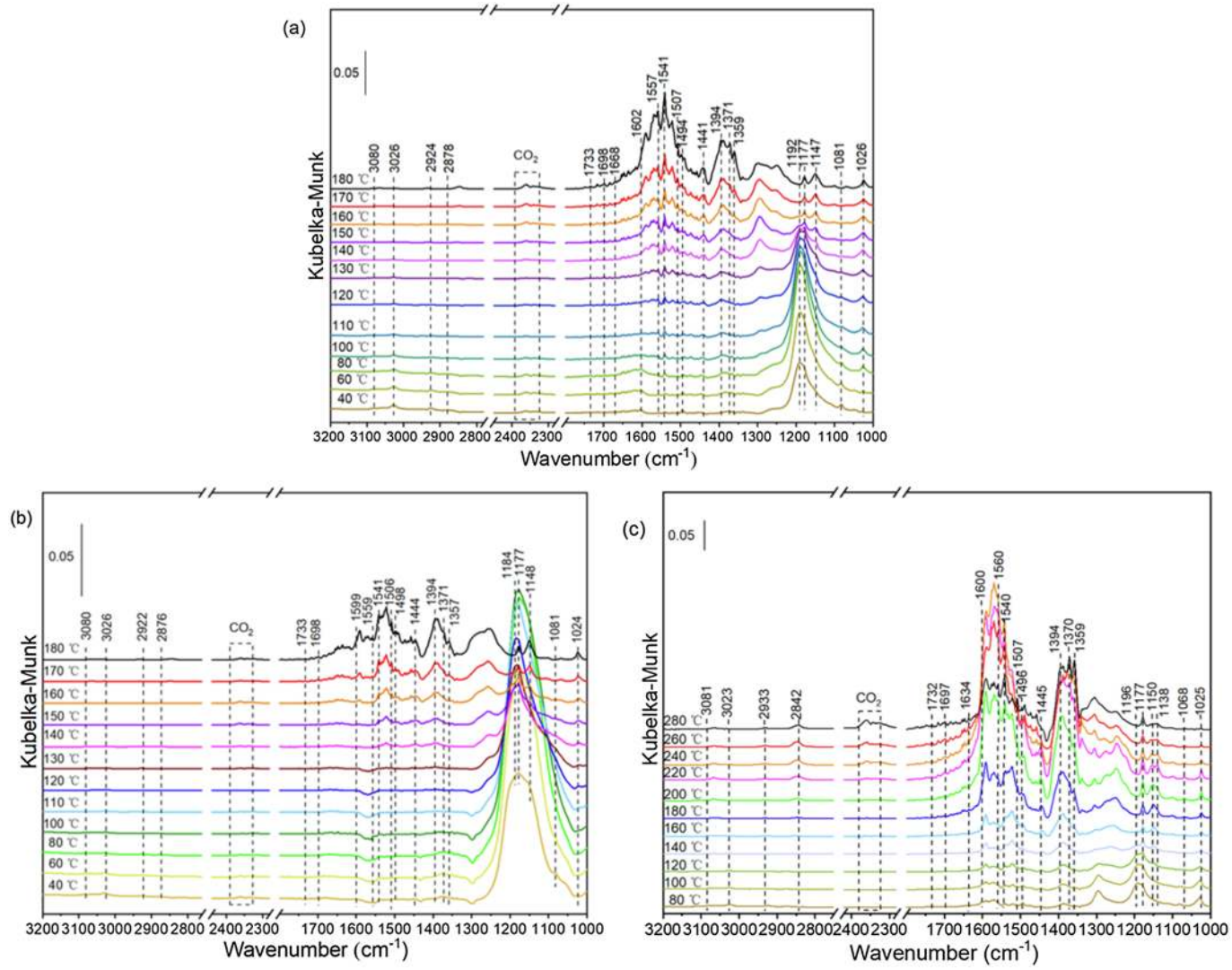

Fig. 7. *In-situ* DRIFTS spectra of 1000 ppm toluene oxidation over (a) $Pt_{2.5}Ir/CeO_2$, (b) Pt/CeO_2, and (c) Ir/CeO_2.

Combined with the results mentioned above, the pathway of toluene oxidation on the Pt/CeO_2 and Ir/CeO_2 showed a similar route with $Pt_{2.5}Ir/CeO_2$. The possible pathway can be concluded as follow: toluene → benzyl alcohol → benzaldehyde → benzoic acid → formate, maleate and acetone → CO_2 and H_2O, shown in Fig. 8. It was worth noting that the benzene ring oping process was the important process [68]. Compared with Pt/CeO_2 (140 °C) and Ir/CeO_2 (160 °C), the benzene ring was broken at lower temperature on the $Pt_{2.5}Ir/CeO_2$ (120 °C), which could be attributed to the active oxygen produced by more Ir^0 species and surface oxygen vacancies. Therefore, with stronger ability to adsorb toluene and activate oxygen, $Pt_{2.5}Ir/CeO_2$ exhibited high catalytic oxidation activity of toluene.

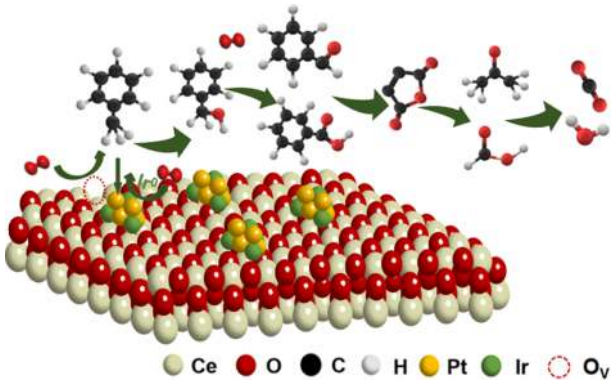

Fig. 8. The reaction pathway of toluene oxidation over Pt_xIr/CeO_2 catalyst.

4. Conclusion

A series of Pt_xIr nano-alloys supported on CeO_2 were successfully prepared by microwave-assisted ethylene glycol reduction method. Pt_xIr alloys were uniformly dispersed on CeO_2. The supported Pt_xIr/CeO_2 catalysts exhibited high catalytic activity for toluene oxidation compared with Pt/CeO_2 and Ir/CeO_2 catalysts. It demonstrated that the interaction between Pt and Ir can be adjusted by change the proportions of Pt and Ir, which can affect the catalytic performance for toluene combustion. The excellent low-temperature catalytic activity over $Pt_{2.5}Ir/CeO_2$ can be attributed to the most of Pt^0 species, Ir^0 species, surface oxygen vacancies and the low-temperature reducibility, as revealed by Raman, XPS and H_2-TPR analysis. *In-situ* DRIFTS investigations showed that the benzene ring of toluene can be broken over $Pt_{2.5}Ir/CeO_2$ at lower temperature compared with monometallic catalysts, promoting the reaction at lower temperature. This finding has significant merit in practice for the efficient removal of VOCs.

CRediT authorship contribution statement

Yue Zhang: Conceptualization, Investigation, Methodology, Validation, Writing – original draft. **Cong Wu:** Investigation, Validation. **Zhiqiang Wang:** Methodology, Formal analysis. **Jiawei Ji:** Software. **Haiqin Wan:** Supervision, Resources, Writing – review & editing, Funding acquisition. **Weixin Zou:** Writing – review & editing. **Qing Tong:** Supervision, Conceptualization, Data curation, Writing – review & editing, Funding acquisition. **Jingfang Sun:** Validation, Formal analysis. **Lin Dong:** Supervision, Project administration, Writing – review & editing. **Yu-Wen Chen:** Writing – review & editing.

Declaration of Competing Interest

The authors declare that they have no known competing financial interests or personal relationships that could have appeared to influence the work reported in this paper.

Acknowledgments

This work was supported by the financial support from the National Natural Science Foundation of China (22106067, 21976082). The National Key Research and Development Program of China (2016YFC0204301) and the Key Research and Development Program of Jiangsu Province of China (BE2019118) are gratefully acknowledged.

Appendix A. Supplementary material

Supplementary data to this article can be found online at https://doi.org/10.1016/j.apsusc.2021.152278.

References

[1] J.Q. Li, H. Liu, Y.Z. Deng, G. Liu, Y.F. Chen, J. Yang, Emerging nanostructured materials for the catalytic removal of volatile organic compounds, Nanotechnol. Rev. 5 (2016) 147–181.
[2] P. Harb, N. Locoge, F. Thevenet, Treatment of household product emissions in indoor air: real scale assessment of the removal processes, Chem. Eng. J. 380 (2020) 122525.
[3] C. He, J. Cheng, X. Zhang, M. Douthwaite, S. Pattisson, Z.P. Hao, Recent advances in the catalytic oxidation of volatile organic compounds: a review based on pollutant sorts and sources, Chem. Rev. 119 (2019) 4471–4568.
[4] Z.Q. Wang, L.X. Zhang, J.W. Ji, Y.W. Wu, Y.D. Cai, X.J. Yao, X.R. Gu, Y. Xiong, H. Q. Wan, L. Dong, Y.W. Chen, Catalytic enhancement of small sizes of CeO_2 additives on Ir/Al_2O_3 for toluene oxidation, Appl. Surf. Sci. 571 (2022) 151200.
[5] S. Ojala, S. Pitkäaho, T. Laitinen, N. Niskalakoivikko, R. Brahmi, J. Gaálová, L. Matejova, A. Kucherov, S. Päivärinta, C. Hirschmann, T. Nevanperä, M. Riihimäki, M. Pirilä, R.L. Keiski, Catalysis in VOC abatement, Top Catal. 54 (2011) 1224.
[6] J.C. Cao, F.G. Wu, M.R. Wen, J.H. Peng, Y. Yang, H.F. Dong, Adsorption mechanism of typical VOCs on pristine and Al-modified MnO_2 monolayer, Appl. Surf. Sci. 539 (2021) 148164.
[7] Y. Jiang, J. Gao, Q. Zhang, Z. Liu, M. Fu, J. Wu, Y. Hu, D. Ye, Enhanced oxygen vacancies to improve ethyl acetate oxidation over MnO_x-CeO_2 catalyst derived from MOF template, Chem. Eng. J. 371 (2019) 78–87.
[8] S. Pitkäaho, L. Matejova, K. Jiratova, S. Ojala, R.L. Keiski, Oxidation of perchloroethylene-Activity and selectivity of Pt, Pd, Rh, and V_2O_5 catalysts supported on Al_2O_3, Al_2O_3-TiO_2 and Al_2O_3-CeO_2, Appl. Catal. B: Environ. 126 (2012) 215–224.
[9] R.S. Peng, S.J. Li, X.B. Sun, Q.M. Ren, L.M. Chen, M.L. Fu, J.L. Wu, D.Q. Ye, Size effect of Pt nanoparticles on the catalytic oxidation of toluene over Pt/CeO_2 catalysts, Appl. Catal. B: Environ. 220 (2018) 462–470.
[10] S.J. Li, Y. Lin, D. Wang, C.H. Zhang, Z. Wang, X.B. Li, Polyhedral cobalt oxide supported Pt nanoparticles with enhanced performance for toluene catalytic oxidation, Chemosphere 263 (2021) 127870.
[11] L.F. Liotta, Catalytic oxidation of volatile organic compounds on supported noble metals, Appl. Catal. B: Environ. 100 (2010) 403–412.
[12] P. Wu, H. Liu, Y. Cao, S. Xi, Z. Li, Z. He, L. Song, J. Xu, P. Bai, L. Zhao, S. Mintova, Z. Yan, Mesostructured cellular foam silica supported Au-Pt nanoalloy: enrichment of d-state electrons for promoting the catalytic synergy, Micropor. Mesopor. Mater. 316 (2021) 110982.
[13] H. Guo, H. Li, K. Jarvis, H. Wan, P. Kunal, S.G. Dunning, Y. Liu, G. Henkelman, S. M. Humphrey, Microwave-assisted synthesis of classically immiscible Ag-Ir alloy nanoparticle catalysts, ACS Catal. 8 (12) (2018) 11386–11397.
[14] H. Guo, Z. Fang, H. Li, D. Fernandez, G. Henkelman, S.M. Humphrey, G. Yu, Rational design of rhodium-iridium alloy nanoparticles as highly active catalysts for acidic oxygen evolution, ACS Nano 13 (11) (2019) 13225–13234.
[15] N. Dahal, S. García, J.P. Zhou, S.M. Humphrey, Beneficial effects of microwave-assisted heating versus conventional heating in noble metal nanoparticle synthesis, ACS Nano 6 (2012) 9433.
[16] X. Fu, Y. Liu, W. Yao, Z. Wu, One-step synthesis of bimetallic Pt-Pd/MCM-41 mesoporous materials with superior catalytic performance for toluene oxidation, Catal. Commun. 83 (2016) 22–26.
[17] W.B. Pei, L.Y. Dai, Y.X. Liu, J.G. Deng, L. Jing, K.F. Zhang, Z.Q. Hou, Z. Han, A. Rastegarpanah, H.X. Dai, PtRu nanoparticles partially embedded in the 3DOM $Ce_{0.7}Zr_{0.3}O_2$ skeleton: Active and stable catalysts for toluene combustion, J. Catal. 385 (2020) 274–288.
[18] J.J. Li, B.L. Zhu, G.C. Wang, Z.F. Liu, W.P. Huang, S.M. Zhang, Enhanced CO catalytic oxidation over an Au-Pt alloy supported on TiO_2 nanotubes: Investigation of the hydroxyl and Au/Pt ratio influences, Catal. Sci. Technol. 8 (2018) 6109–6122.
[19] M. Okumura, N. Masuyama, E. Konishi, S. Ichikawa, T. Akita, CO oxidation below room temperature over Ir/TiO_2 catalyst prepared by deposition precipitation method, J. Catal. 208 (2) (2002) 485–489.
[20] X.C. Sun, J. Lin, Y.H. Wang, L. Li, X.L. Pan, Y. Su, X.D. Wang, Catalytically active Ir^0 species supported on Al_2O_3 for complete oxidation of formaldehyde at ambient temperature, Appl. Catal. B: Environ. 268 (2020) 118741.
[21] H. Ohtsuka, The oxidation of methane at low temperatures over zirconia-supported Pd, Ir and Pt catalysts and deactivation by sulfur poisoning, Catal. Lett. 141 (3) (2011) 413–419.
[22] L. Torrente-Murciano, B. Solsona, S. Agouram, R. Sanchis, J.M. López, T. García, R. Zanella, Low temperature total oxidation of toluene by bimetallic Au-Ir catalysts, Catal. Sci. Technol. 7 (13) (2017) 2886–2896.
[23] Q. Fu, H. Saltsburg, M. Flytzani-Stephanopoulos, Active monometallic Au and Pt species on ceria-based water-gas shift catalysts, Science 301 (2003) 935–938.
[24] H. Guo, H. Li, D. Fernandez, S. Willis, K. Jarvis, G. Henkelman, S.M. Humphrey, Stabilizer-free CuIr alloy nanoparticle catalysts, Chem. Mater. 31 (24) (2019) 10225–10235.
[25] Y. Xia, L.u. Xia, Y. Liu, T. Yang, J. Deng, H. Dai, Concurrent catalytic removal of typical volatile organic compound mixtures over Au-Pd/α-MnO_2 nanotubes, J. Environ. Sci. 64 (2018) 276–288.
[26] S.H. Xie, Y.X. Liu, J.G. Deng, X.T. Zhao, J. Yang, K.F. Zhang, Z. Han, H.X. Dai, Three-dimensionally ordered macroporous CeO_2-supported Pd@Co nanoparticles: Highly active catalysts for methane oxidation, J. Catal. 342 (2016) 17–26.
[27] B.X. Chen, B.F. Wang, Y.H. Sun, X.Q. Wang, M.L. Wu, L.M. Chen, Y.F. Tam, D. Q. Ye, Plasma-assisted surface interactions of Pt/CeO_2 catalyst for enhanced toluene catalytic oxidation, Catalysts 9 (2018) 2.
[28] Z. Wu, M. Li, J. Howe, H.M. Meyer, S.H. Overbury, Probing defect sites on CeO_2 nanocrystals with well-defined surface planes by Raman spectroscopy and O_2 adsorption, Langmuir 26 (21) (2010) 16595–16606.
[29] X. Zhang, L. Dai, Y. Liu, J. Deng, L. Jing, X. Yu, Z. Han, K. Zhang, H. Dai, 3DOM CeO_2-supported RuyM (M = Au, Pd, Pt) alloy nanoparticles with improved catalytic activity and chlorine-tolerance in trichloroethylene oxidation, Catal. Sci. Technol. 10 (11) (2020) 3755–3770.
[30] J. Kašpar, P. Fornasiero, M. Graziani, Use of CeO_2-based oxides in the three-way catalysis, Catal. Today 50 (1999) 285–298.
[31] L. Liu, Z. Yao, Y.u. Deng, F. Gao, B. Liu, L. Dong, Morphology and crystal-plane effects of nanoscale ceria on the activity of CuO/CeO_2 for NO reduction by CO, ChemCatChem 3 (6) (2011) 978–989.
[32] Y.S. Huang, S.S. Lin, C.R. Huang, M.C. Lee, T.E. Dann, F.Z. Chien, Raman spectrum of IrO_2, Solid State Commun. 70 (5) (1989) 517–522.
[33] L. Schick, R. Sanchis, V. González-Alfaro, S. Agouram, J.M. López, L. Torrente-Murciano, T. García, B. Solsona, Size-activity relationship of iridium particles supported on silica for the total oxidation of volatile organic compounds (VOCs), Chem. Eng. J. 366 (2019) 100–111.
[34] X. Zhang, Y.X. Liu, J.G. Deng, X.H. Yu, Z. Han, K.F. Zhang, H.X. Dai, Alloying of gold with palladium: An effective strategy to improve catalytic stability and chlorine-tolerance of the 3DOM CeO_2-supported catalysts in trichloroethylene combustion, Appl. Catal. B: Environ. 257 (2019) 117879.
[35] H. Arandiyan, H.X. Dai, K.M. Ji, H.Y. Sun, J.H. Li, Pt Nanoparticles embedded in colloidal crystal template derived 3D ordered macroporous $Ce_{0.6}Zr_{0.3}Y_{0.1}O_2$: Highly efficient catalysts for methane combustion, ACS Catal. 5 (2015) 1781–1793.
[36] G.Q. Li, C.H. Zhang, Z. Wang, H. Huang, H. Peng, X.B. Li, Fabrication of mesoporous Co_3O_4 oxides by acid treatment and their catalytic performances for toluene oxidation, Appl. Catal. A: Gen. 550 (2018) 67–76.
[37] Y. Wang, H. Arandiyan, J. Scott, M. Akia, H. Dai, J. Deng, K.-F. Aguey-Zinsou, R. Amal, High performance Au-Pd supported on 3D hybrid strontium-substituted lanthanum manganite perovskite catalyst for methane combustion, ACS Catal. 6 (10) (2016) 6935–6947.
[38] W.X. Zhang, S. Xia, C.L. Chen, H.H. He, Z.N. Jin, M.F. Luo, J. Chen, Understanding the crucial roles of catalyst properties on ethyl acetate and toluene oxidation over Pt catalysts, New J. Chem. 45 (2021) 11352–11358.
[39] H.C. Chan, T. Chen, L. Xie, Y. Shu, Q. Gao, Enhancing formaldehyde oxidation on iridium catalysts using hydrogenated TiO_2 supports, New J. Chem. 42 (22) (2018) 18381–18387.
[40] W. Feng, G. Wu, L. Li, N. Guan, Solvent-free selective photocatalytic oxidation of benzyl alcohol over modified TiO_2, Green Chem. 13 (11) (2011) 3265.
[41] K. Tang, Z. Wang, W. Zou, H. Guo, Y. Wu, Y.u. Pu, Q. Tong, H. Wan, X. Gu, L. Dong, J. Rong, Y.-W. Chen, Advantageous role of Ir^0 supported on TiO_2 nanosheets in

photocatalytic CO_2 reduction to CH_4: Fast electron transfer and rich surface hydroxyl groups, ACS Appl. Mater. Interfaces 13 (5) (2021) 6219–6228.
[42] B. Ledesma, J. Juárez, J. Mazarío, M. Domine, A. Beltramone, Bimetallic platinum/iridium modified mesoporous catalysts applied in the hydrogenation of HMF, Catal. Today 360 (2021) 147–156.
[43] V.A. Valles, B.C. Ledesma, L.P. Rivoira, J. Cussa, O.A. Anunziata, A.R. Beltramone, Experimental design optimization of the tetralin hydrogenation over Ir-Pt-SBA-15, Catal. Today 271 (2016) 140–148.
[44] Y. Li, X. Chen, C. Wang, C. Zhang, H. He, Sodium enhances Ir/TiO_2 activity for catalytic oxidation of formaldehyde at ambient temperature, ACS Catal. 8 (12) (2018) 11377–11385.
[45] S. Cao, X.Q. Fei, Y.X. Wen, Z.X. Sun, H.Q. Wang, Z.B. Wu, Bimodal mesoporous TiO_2 supported Pt, Pd and Ru catalysts and their catalytic performance and deactivation mechanism for catalytic combustion of Dichloromethane (CH_2Cl_2), Appl. Catal. A: Gen. 550 (2018) 20–27.
[46] H.M. Qin, X.S. Qian, M. Tao, Y. Lin, Z. Ma, Pt/MO_x/SiO_2, Pt/MO_x/TiO_2, and Pt/MO_x/Al_2O_3 catalysts for CO oxidation, Catalysis 5 (2015) 606–633.
[47] J. Prabhuram, T.S. Zhao, C.W. Wong, J.W. Guo, Synthesis and physical/electrochemical characterization of Pt/C nanocatalyst for polymer electrolyte fuel cells, J. Power Sources 134 (1) (2004) 1–6.
[48] C. He, Z. Jiang, M. Ma, X. Zhang, M. Douthwaite, J.-W. Shi, Z. Hao, Understanding the promotional effect of Mn_2O_3 on micro-/mesoporous hybrid silica nanocubic-supported Pt catalysts for the low-temperature destruction of methyl ethyl ketone: An experimental and theoretical study, ACS Catal. 8 (5) (2018) 4213–4229.
[49] C. Chen, F. Chen, L. Zhang, S. Pan, C. Bian, X. Zheng, X. Meng, F.-S. Xiao, Importance of platinum particle size for complete oxidation of toluene over Pt/ZSM-5 catalysts, Chemi. Commun. 51 (27) (2015) 5936–5938.
[50] Y. Huang, Y. Ma, Y. Cheng, L. Wang, X.i. Li, Supported nanometric platinum-nickel catalysts for solvent-free hydrogenation of tetralin, Catal. Commun. 69 (2015) 55–58.
[51] Q.i. Zhang, S. Mo, J. Li, Y. Sun, M. Zhang, P. Chen, M. Fu, J. Wu, L. Chen, D. Ye, In situ DRIFT spectroscopy insights into the reaction mechanism of CO and toluene co-oxidation over Pt-based catalysts, Catal. Sci. Technol. 9 (17) (2019) 4538–4551.
[52] W. Tan, H. Alsenani, S.H. Xie, Y.D. Cai, P. Xu, A.N. Liu, J.W. Ji, F. Gao, L. Dong, E. Chukwu, M. Yang, F.D. Liu, Tuning Single-atom Pt_1-CeO_2 catalyst for efficient CO and C_3H_6 oxidation: size effect of ceria on Pt structural evolution, ChemNanoMat 6 (2020) 1797–1805.
[53] B.F. Wang, B.X. Chen, Y.H. Sun, H.L. Xiao, X.X. Xu, M.L. Fu, J.L. Wu, L.M. Chen, D. Q. Ye, Effects of dielectric barrier discharge plasma on the catalytic activity of Pt/CeO_2 catalysts, Appl. Catal. B: Environ. 238 (2018) 328–338.
[54] Y.J. Huang, J. Xue, J.A. Schwarz, Analysis of temperature-programmed reduction profiles from metal-supported catalysts, J. Catal. 111 (1988) 59–66.
[55] S. Besselmann, E. Löffler, M. Muhler, On the role of monomeric vanadyl species in toluene adsorption and oxidation on V_2O_5/TiO_2 catalysts: a Raman and in situ DRIFTS study, J. Mol. Catal. A: Chem. 162 (1-2) (2000) 401–411.
[56] Y. Liao, X. Zhang, R. Peng, M. Zhao, D. Ye, Catalytic properties of manganese oxide polyhedra with hollow and solid morphologies in toluene removal, Appl. Surf. Sci. 405 (2017) 20–28.
[57] S.P. Mo, J. Li, R.Q. Liao, P. Peng, J.J. Li, J.L. Wu, M.L. Fu, L. Liao, T.M. Shen, Q. L. Xie, D.Q. Ye, Unravelling the decisive role of surface CeO_2 nanoparticles in the Pt-CeO_2/MnO_2 hetero-catalysts for boosting toluene oxidation: synergistic effect of surface decorated and intrinsic O-vacancies, Chem. Eng. J. 418 (2021) 129399.
[58] P. Liu, Y. Liao, J. Li, L. Chen, M. Fu, P. Wu, R. Zhu, X. Liang, T. Wu, D. Ye, Insight into the effect of manganese substitution on mesoporous hollow spinel cobalt oxides for catalytic oxidation of toluene, J. Colloid Interf. Sci. 594 (2021) 713–726.
[59] Z.Q. Wang, P.J. Ma, K. Zheng, C. Wang, Y.X. Liu, H.X. Dai, C.C. Wang, H.C. Hsi, J. G. Deng, Size effect, mutual inhibition and oxidation mechanism of the catalytic removal of a toluene and acetone mixture over TiO_2 nanosheet-supported Pt nanocatalysts, Appl. Catal. B: Environ. 274 (2020) 118963.
[60] J. Huang, R.M. Fang, Y.J. Sun, J.Y. Li, F. Dong, Efficient α-MnO_2 with (2 1 0) facet exposed for catalytic oxidation of toluene at low temperature: a combined in-situ DRIFTS and theoretical investigation, Chemosphere 263 (2021) 128103.
[61] X. Yang, X. Yu, M. Jing, W. Song, J. Liu, M. Ge, Defective $Mn_xZr_{1-x}O_2$ solid solution for the catalytic oxidation of toluene: Insights into the oxygen vacancy contribution, ACS Appl. Mater. Interfaces 11 (1) (2019) 730–739.
[62] Z. Rui, M. Tang, W. Ji, J. Ding, H. Ji, Insight into the enhanced performance of TiO_2 nanotube supported Pt catalyst for toluene oxidation, Catal. Today 297 (2017) 159–166.
[63] R. Mendezromán, N. Cardonamartínez, Relationship between the formation of surface species and catalyst deactivation during the gas-phase photocatalytic oxidation of toluene, Catal. Today 40 (1998) 353–365.
[64] A. Lu, H. Sun, N. Zhang, L. Che, S. Shan, J. Luo, J. Zheng, L. Yang, D.-L. Peng, C.-J. Zhong, B. Chen, Surface partial-charge-tuned enhancement of catalytic activity of platinum nanocatalysts for toluene oxidation, ACS Catal. 9 (8) (2019) 7431–7442.
[65] M.D. Hernándezalonso, I. Tejedortejedor, J.M. Coronado, M.A. Anderson, Operando FTIR study of the photocatalytic oxidation of methylcyclohexane and toluene in air over TiO_2-ZrO_2 thin films: Influence of the aromaticity of the target molecule on deactivation, Appl. Catal. B: Environ. 101 (2011) 283–293.
[66] W. Yang, Y. Peng, Y.a. Wang, Y. Wang, H. Liu, Z. Su, W. Yang, J. Chen, W. Si, J. Li, Controllable redox-induced in-situ growth of MnO_2 over Mn_2O_3 for toluene oxidation: active heterostructure interfaces, Appl. Catal. B: Environ. 278 (2020) 119279.
[67] Z.W. Wang, H.G. Yang, R.L. Liu, S.H. Xie, Y.X. Liu, H.X. Dai, H.B. Huang, J.G. Deng, Probing toluene catalytic removal mechanism over supported Pt nano- and single-atom-catalyst, J. Hazard. Mater. 392 (2020) 122258.
[68] K. Yu, J. Deng, Y.J. Shen, A.Y. Wang, L.Y. Shi, D.S. Zhang, Efficient catalytic combustion of toluene at low temperature by tailoring surficial Pt^0 and interfacial Pt-$Al(OH)_x$ species, iScience 24 (2021) 102689.